Geochemistry Geophysics Geosystems G3
AN ELECTRONIC JOURNAL OF THE EARTH SCIENCES
Published by AGU and the Geochemical Society

Article
Volume 9, Number 11
6 November 2008
Q11001, doi:10.1029/2008GC002069
ISSN: 1525-2027

Multiarrival wavefront tracking and its applications

J. Hauser, M. Sambridge, and N. Rawlinson
Research School of Earth Sciences, Australian National University, Canberra, ACT 0200, Australia (nick@rses.anu.edu.au)

[1] Multivalued traveltimes have traditionally not been used in seismic imaging, with only a handful of notable exceptions in the field of exploration geophysics. For studies at local and regional scales (e.g., local earthquake/teleseismic tomography), the focus has largely been on first arrivals, with numerous ray- and grid-based schemes developed for their calculation. However, later arrivals often contribute to the length and shape of a recorded wave train, particularly in regions of complex geology. These arrivals are likely to contain additional information about seismic structure, as their two point path differs from that of the first arrival; in particular, they are more amenable to sampling regions of lower velocity. In this work the wavefront construction principle is used as the basis of a new scheme for computing multivalued traveltimes that arise from smooth variations in both velocity structure and interface geometry. The idea is to represent the wavefront as a set of points in reduced phase space and use local ray tracing and interpolation to advance the wavefront in a series of time steps. The scheme is robust in the presence of strong velocity heterogeneity and interface curvature, with phases comprising multiple reflections, refractions, and triplications successfully tracked. Outside the field of exploration seismology wavefront construction techniques are rarely used, yet they hold great potential for addressing problems in other areas of seismology. This paper demonstrates the viability of the new wavefront construction scheme by applying it to a range of scenarios, including multiarrival body and surface wave tomography, teleseismic receiver function prediction using Gaussian beams, and the tracking of global phases such as *PcP*.

Components: 10,683 words, 18 figures, 1 table.

Keywords: wavefront tracking; multiarrival tomography; surface waves.

Index Terms: 7270 Seismology: Tomography (6982, 8180); 7203 Seismology: Body waves; 7255 Seismology: Surface waves and free oscillations.

Received 22 April 2008; **Revised** 1 September 2008; **Accepted** 22 September 2008; **Published** 6 November 2008.

Hauser, J., M. Sambridge, and N. Rawlinson (2008), Multiarrival wavefront tracking and its applications, *Geochem. Geophys. Geosyst.*, *9*, Q11001, doi:10.1029/2008GC002069.

1. Introduction

[2] The calculation of ray traveltimes through a medium with a heterogeneous velocity distribution still remains the foundation of many applications that rely on the high-frequency component of seismic records, such as body wave tomography, migration of reflection data, and earthquake relocation [e.g., *Thurber*, 1983; *Gray and May*, 1994; *Hammer et al.*, 1994; *Steck et al.*, 1998]. Despite many decades of technique development [e.g., *Julian and Gubbins*, 1977; *Vidale*, 1988; *Sethian and Popovici*, 1999], there is still no single method that can accurately, efficiently, and robustly overcome the nonlinearity of the two point problem and compute multiarrivals in complex media. The aim

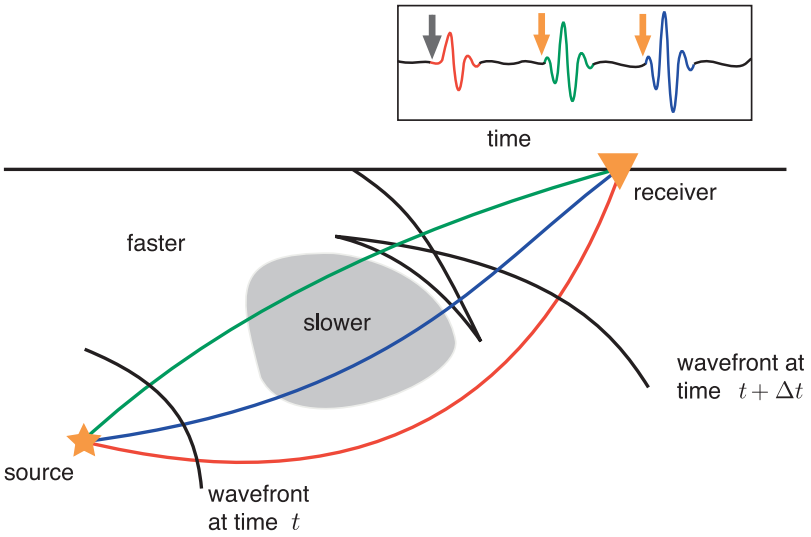

Figure 1. Schematic diagram showing ray paths for a medium containing a slow velocity anomaly. The wavefront triplicates and three arrivals are observed. The ray path for the first, second, and third arrivals are shown in red, green, and blue, respectively.

of this paper is to advance the current state of the art in seismic wavefront tracking in two dimensions for heterogeneous media and to investigate the potential of multiarrival information for improving various seismic applications including tomography.

[3] Both continuous and discontinuous variations in wave speed can cause seismic energy to travel to a receiver along more than one path, a phenomenon commonly referred to as multipathing. This is illustrated in Figure 1 where a wavefront triplicates due to the presence of a low-velocity anomaly, resulting in the detection of three separate arrivals at the receiver. The shape of the self-intersecting wavefront at time $t + \Delta t$ resembles what is often described as a swallowtail. The first arrival path avoids the low-velocity anomaly, which is subsequently sampled by the second and third arrival. Clearly, later arrivals sample different parts of the medium and therefore should carry additional structural information. However, most practical algorithms for tracking wavefronts can only provide the traveltimes of first arrivals [e.g., *Rawlinson and Sambridge*, 2004a; *Buske and Kästner*, 2004; *de Kool et al.*, 2006]. While it is true that standard ray tracing methods can locate later arrivals, their reliability in doing so rapidly decreases as the complexity of the medium increases (for an effective demonstration, see Figure 32 of *Rawlinson et al.* [2007]). As such, they cannot be viewed as viable techniques for the routine prediction of multipathing. The development of advanced and computationally practical schemes for tracking multiple arrivals through complex two- and three-dimensional media would allow the prediction of many more observable phases, which has the potential to benefit many areas of seismology.

[4] Traditionally, the method of choice for the computation of traveltimes has been ray tracing, i.e., computing the characteristics of the eikonal equation. [e.g., *Julian and Gubbins*, 1977; *Pereyra et al.*, 1980; *Zelt and Ellis*, 1988; *Virieux and Farra*, 1991; *Červený*, 2001]. Ray tracing between a source and receiver can be achieved by shooting or bending rays. The shooting method relies on repeated solution of an initial value problem in order to locate two point paths. Rays are initiated at the source point with different initial directions and tracked through the medium by solving the appropriate initial value formulation of the ray tracing equation [e.g., *Červený et al.*, 1977; *Červený*, 2001]. This step is highly accurate and efficient, even in the presence of interfaces, and allows various seismic wave properties, like geometrical spreading, attenuation, and amplitudes, to be predicted. It is also possible to compute synthetic seismograms, based on seismic properties calculated along the rays, using techniques like the Gaussian beam method [*Červený and Pšenčík*, 1984] or Maslov integration [*Chapman*, 1985].

[5] The challenge, however, is to determine the initial direction vector of the ray that will hit a particular receiver. This two point problem of finding a source-receiver ray path can be formulated as an optimization problem, in which the

unknown is the initial direction vector of the ray, and the function to be minimized is a measure of the distance between the ray endpoint and receiver. Since the optimization problem is nonlinear, a range of iterative nonlinear and fully nonlinear schemes have been employed [e.g., *Julian and Gubbins*, 1977; *Sambridge and Kennett*, 1990; *Virieux and Farra*, 1991; *Velis and Ulrych*, 1996].

[6] A common alternative to tracing rays is to compute the first arrival traveltime to all nodes of a grid which spans the medium [e.g., *Vidale*, 1988; *van Trier and Symes*, 1991; *Kim and Cook*, 1999; *Sethian and Popovici*, 1999]. The resulting traveltime field implicitly contains the wavefront location as a function of time (i.e., isochrons of the traveltime field), and all possible first arrival ray paths are given by the gradient of the traveltime field. In these Eulerian schemes the wavefront is tracked implicitly. Grid-based methods have evolved to the point where many can guarantee to locate the first arrival traveltime and ray path to all points of the medium [e.g., *Rawlinson and Sambridge*, 2004a; *Buske and Kästner*, 2004], even for highly heterogeneous media, where boundary value ray tracing is likely to perform poorly.

[7] The question of whether or not first arrivals are sufficient for imaging complex structures was posed soon after the appearance of first arrival finite difference techniques. In the context of exploration geophysics, *Geoltrain and Brac* [1993] conjectured that most of the wavefield energy is contained in later arrivals and therefore first arrival traveltimes are not sufficient to give a good migration image. There have been attempts to compute multivalued traveltime fields using only a first arrival solver. However, these schemes often include a rather ad hoc procedure for dividing the computational domain into single valued subregions, followed by application of a first arrival solver in each subregion. The solutions for the different subregions are then superimposed to construct the multivalued traveltime field [e.g., *Fatemi et al.*, 1995; *Benamou*, 1999].

[8] In this work wavefront tracking refers to schemes in which the wavefront is described explicitly (i.e., by a set of points and not as the isochron of a traveltime field). These Lagrangian approaches to the problem of seismic wavefront tracking were introduced in two dimensions by *Lambaré et al.* [1992] and *Vinje et al.* [1993] and in three dimensions by *Vinje et al.* [1999]. The advantage of explicit wavefront tracking is that it can be used to track all arrivals of a wavefront. The basic principle is that a wavefront can be evolved by repeated applications of local ray tracing to a set of points lying on the wavefront. New points can be interpolated at each step to overcome the undersampling problems that may arise as the wavefront expands and distorts due to velocity heterogeneity. Redundant points could also be removed to improve efficiency, but to date, no published wavefront tracking scheme has implemented such a procedure.

[9] We begin by introducing the concept of a reduced phase space distance criteria for maintaining a fixed density of points on the wavefront. In reduced phase space, a triplicating wavefront unravels into a smooth curve, which makes adding and removing points a much more straightforward task. This forms the core of our multiarrival wavefront tracking algorithm. We then discuss how arrival times and ray paths can be extracted once the wavefront tracking is completed. Multiarrival wavefront tracking is then combined with the Gaussian beam method, which traditionally relies on ray tracing to compute all arrivals. We conclude by discussing the potential of multiarrival tomography using body wave or surface wave data sets.

2. Method

[10] The idea of explicitly tracking a wavefront by advancing a set of points using local ray tracing and interpolation has been investigated over the last decade and half, mainly in the exploration seismology field [e.g., *Vinje et al.*, 1993; *Lambaré et al.*, 1996; *Buske and Kästner*, 2004]. However, in these earlier studies, ray density has been defined only in normal space, for example, the metric distance between neighboring rays [*Lambaré et al.*, 1992; *Vinje et al.*, 1993; *Ettrich and Gajewski*, 1996] or the angular distance [*Sun*, 1992]. These definitions of ray density tend to encounter difficulties if the wavefront starts to develop a swallowtail pattern; they are only loosely correlated to the complexity of the ray field. In this work ray density is measured using a metric defined in reduced phase space.

2.1. Reduced Phase Space

[11] Wavefront tracking in phase space using a Lagrangian framework has been done previously by *Lambaré et al.* [1996] and *Lucio et al.* [1996] using the Hamiltonian formulation of ray theory. For a wavefront in two-dimensional real space (or normal space) a four-dimensional phase space can

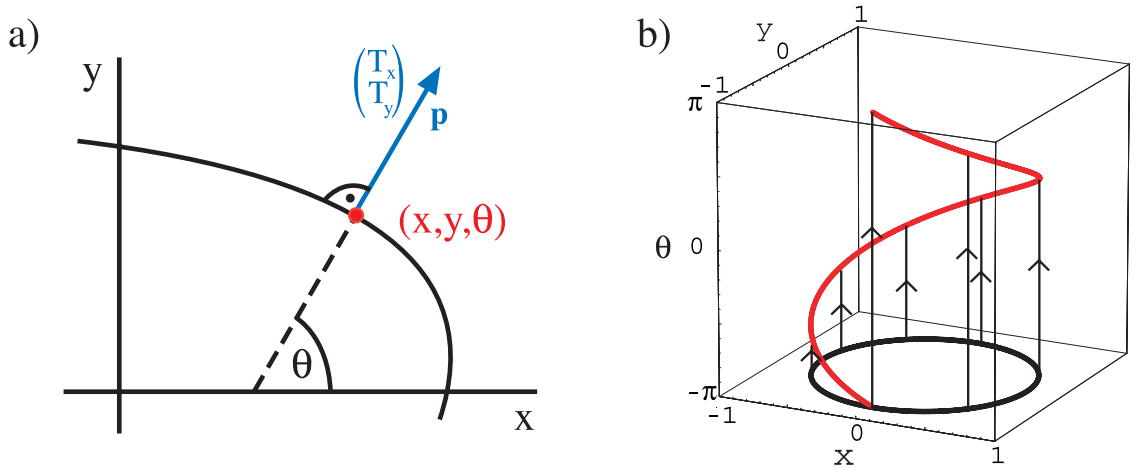

Figure 2. Reduced phase space representation of a two-dimensional wavefront. (a) Ray trajectory from the wavefront supplies third dimension θ. (b) Wavefront in normal space (black line) and corresponding bicharacteristic strip (red line) in reduced phase space.

be constructed where the four coordinates are the two components of the position vector and the slowness vector. The characteristics of the eikonal equation in phase space are given by [e.g., *Červený*, 2001; *Chapman*, 2004]

$$\frac{d\mathbf{x}}{dt} = c\frac{\mathbf{p}}{|\mathbf{p}|}, \qquad \frac{d\mathbf{p}}{dt} = -|\mathbf{p}|\nabla c, \tag{1}$$

where $\mathbf{p} = \nabla T$ is the slowness vector, $\mathbf{x}$ is the position vector in real space, c is the speed, and t is the time. This is the Hamiltonian formulation of ray theory, where the rays are the bicharacteristics in ($\mathbf{x}$, ∇T) (or just characteristics in $\mathbf{x}$) and the wavefront is generally known as the bicharacteristic strip [e.g., *Chapman*, 1985; *Osher et al.*, 2002]. It defines the direction and location of the wavefront.

[12] Instead of using four-dimensional phase space it is also possible to define a reduced phase space [e.g., *Osher et al.* 2002] which is three-dimensional for a wavefront in two-dimensional real space. The third component is defined by the angle the slowness vector forms with the x axis (see Figure 2). The two components of the slowness vector describing the motion of a node on the wavefront T_x and T_y are essentially combined into θ, the direction of the local wavefront normal or slowness vector, using the relationship $\tan\theta = (T_y/T_x)$.

[13] To transform a wavefront from two-dimensional real space into three-dimensional reduced phase space, one can calculate the direction θ of the local wavefront normal and use it as the third coordinate. The bicharacteristic strip will therefore not self-intersect as two intersecting rays will always propagate in different directions, i.e., have different θ values. The other advantage of reduced phase space is that wavefronts containing sharp corners will be described by a locally smooth bicharacteristic strip (see Figure 3). Whenever the position of the wavefront is required, the bicharacteristic strip is mapped back into normal space. The use of a phase space distance metric is a key element of the Lagrangian method employed here and is superior to the alternative of using a metric defined in normal space. *Lambaré et al.* [1996] use a similar criterion for the ray density in phase space within their Hamiltonian formulation of ray theory.

[14] The bicharacteristic strip is evolved through the medium in a series of discrete time steps. For a given time step Δt, the strip is updated using a two-stage procedure. In the first stage, all points are evolved in time by using a fourth-order Runge Kutta solver [e.g., *Press et al.*, 1992] for the following initial value formulation of the kinematic ray tracing equation [e.g., *Červený*, 2001]:

$$\frac{dx}{dt} = c\cos\theta, \qquad \frac{dy}{dt} = c\sin\theta, \qquad \frac{d\theta}{dt} = c_x\sin\theta - c_y\cos\theta, \tag{2}$$

where $c(x, y)$ defines the wave speed, c_x and c_y are its derivatives in the x and y direction, respectively, and θ is the inclination angle of the ray at (x, y). Surface waves can be tracked by using the system

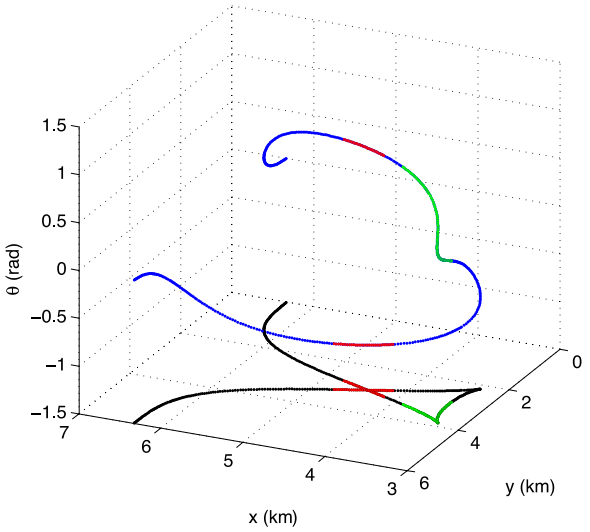

Figure 3. Swallowtail pattern of a wavefront. The sharp corners in normal space (green segments) are given by a smooth representation in reduced phase space. The intersecting segments in normal space (red lines) do not intersect each other in reduced phase space.

of equations for kinematic ray tracing on a sphere [e.g., *Červený*, 2001; *Aki and Richards*, 2002; *Bukchin et al.*, 2006].

[15] Smooth variations in wave speed $c(x, y)$ are defined by a mosaic of cubic B-spline area elements, the values of which are determined by a regular mesh of control vertices. The benefit of cubic B-spline functions is that the first and second derivatives of the resulting field are continuous and given by an analytical expression.

[16] Once all points along the bicharacteristic strip at time t have been updated to the new strip at time $t + \Delta t$, points can then be added or removed depending on their separation in reduced phase space. The aim is to keep a fixed density of points along the bicharacteristic strip in order to minimize the loss of detail as the wavefront progresses through the medium. As the evolving wavefront distorts in response to velocity heterogeneity, points may also cluster together, resulting in oversampling. It is therefore desirable to allow points to be removed, as it will increase the accuracy to computation time ratio.

[17] If σ represents the initial distance between adjacent points along the bicharacteristic strip, then a new point is added if the distance between two neighboring points exceeds 2σ, and an existing point is removed if the distance falls below $\sigma/2$. The position of a new point in reduced phase space is determined using linear or higher-order interpolation between its two neighbors. Using a factor of 2 means that the point density will stay close to the initial value during the propagation of the bicharacteristic strip. For the calculation of the distance between two neighboring points, the two metric coordinates x and y are normalized to lie in the same range as θ (i.e., in $[-\pi, +\pi]$). This scaling allows the norm distance measure in reduced phase space to be defined and hence the point density.

[18] Figure 4 illustrates the advantage of using the concept of a phase space distance for the refinement compared to angular or metric distance used in normal space. Here a plane wave enters the medium from the bottom and propagates to the top. Clearly, the endpoints of the swallowtail are distorted when the metric distance is used to decide when to add or remove points but well represented when the reduced phase space distance is employed.

2.2. Interfaces

[19] Discontinuities in the velocity field, for example the boundary of a salt dome or the Moho, give rise to another class of phase in the form of reflected and refracted wavefronts. These wavefronts may be multivalued, if the impinging wavefront is multivalued, or if the geometry of the interface is such that significant focusing or defo-

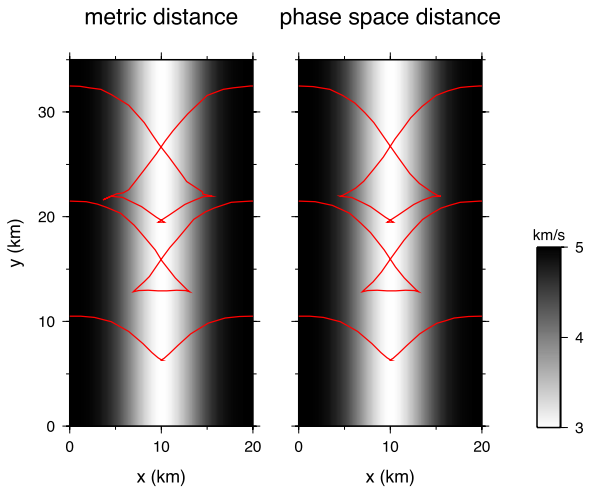

Figure 4. A plane wave parallel to the x axis at $y = 0$ propagates in the positive y direction. The wavefront begins to triplicate and forms a swallowtail due to the low velocity in the center. (right) When the reduced phase space distance is used as a criterion for adding points, the swallowtail pattern is better recovered compared to when (left) the metric distance is used. The initial plane wave is in both cases represented using 25 points.

cusing occurs. In the following treatment, the Lagrangian scheme is extended so that it can be used to compute multivalued traveltimes in the presence of interfaces.

2.2.1. Interface Representation

[20] In this work, interfaces are defined by a set of control points with cubic B-splines used to describe the position of the interface as a function of incremental path length. This allows overturning boundaries and isolated bodies to be represented.

[21] A regular grid of nodes coupled with cubic B-splines is used to describe smoothly varying velocity fields within both layers and isolated bodies. This concept of assigning an individual velocity grid to each layer can be extended by using two velocity grids for each layer, one for *P* waves and one for *S* waves, which allows mode conversions.

2.2.2. Wavefront Propagation in the Presence of Interfaces

[22] If there are multiple layers present, a natural approach for tracking the wavefront is to consider its propagation in each layer separately. Such a multistage method for computing traveltimes in a layered model has also been used by *Rawlinson and Sambridge* [2004b], in the context of implicit wavefront tracking with the fast marching method.

[23] Figure 5 illustrates the multistage approach used in this work. When the position of a point on the bicharacteristic strip is updated for a given time step, a check is made to see whether a portion of the path between its current and previous position lies in a grid cell which contains an interface. If the ray crosses the interface, an intersection point is calculated. Having finished the propagation of a wavefront in a given layer, all the points have either left the computational domain or are lying on an interface. In the latter case the arrival time, angle of incidence, and local direction of the interface normal are known, so a reflected or refracted wave can be initialized. Following application of Snell's law, the starting position and time of each point of the departing bicharacteristic strip is now known.

[24] In practical applications traveltimes and rays are needed for a limited set of paths. In our scheme a path is defined by a set of segments, where each segment contains information about the wavefront to be tracked in a given layer, i.e., the origin of the wavefront (source point or an interface), the type of wave (*P*, *SV*, or *SH* and direct, reflected, or refracted), and its destination (an interface identifier). In conventional ray tracing methods this type of phase identification is often referred to as a path signature or a ray code [e.g., *Červený*, 2001]. For any path signature the new scheme computes first and later arrivals if they exist. This means that a path signature may represent a family of rays between source and receiver, as illustrated in Figure 5 where the three red rays have the same path signature but different arrival times and propagation paths.

[25] When several path signatures are specified for a particular source, the paths often differ from each other only after a number of reinitialization steps. Every path will, for example, require the wavefront which propagates through the region in which the source is located. In order to avoid having to recompute wavefronts, a tree structure containing all the wavefronts needed for the different path signatures is built (see Figure 5). As shown in Figure 5, the wavefront for certain path signatures may have gaps (i.e., a shadow zone). In this case, not every point on the surface can be reached by a ray which bounces off the lower boundary and then refracts at the upper boundary of the middle layer (see Figure 5, stage 2b).

2.3. Extracting Arrival Information

[26] In most practical applications, the source-receiver traveltime, and in many cases the associated ray paths, are needed rather than the wavefronts. The main challenge in extracting this information is to locate the receiver in an irregular and potentially multivalued traveltime field. Since the wavefront is explicitly defined at each time step, it is possible to identify the two consecutive wavefronts at times t and $t + \Delta t$ and the adjacent ray paths that together bound a receiver. Using the two wavefronts and the associated ray path segments between the points on the wavefront a set of adjacent polygons can be defined. The problem of calculating an arrival time at a receiver then becomes one of identifying the polygon in which a receiver is located.

[27] Testing whether a point lies inside a polygon is a basic operation in computer graphics. The approach adopted in this work is the so-called crossing method [*Haines*, 1994], where one traces a line from the receiver horizontally (increasing x and constant y) and counts how many edges it crosses. If the number of edges crossed is even, the point lies outside the polygon; if it is odd, the point lies inside the polygon. If it has been determined that a

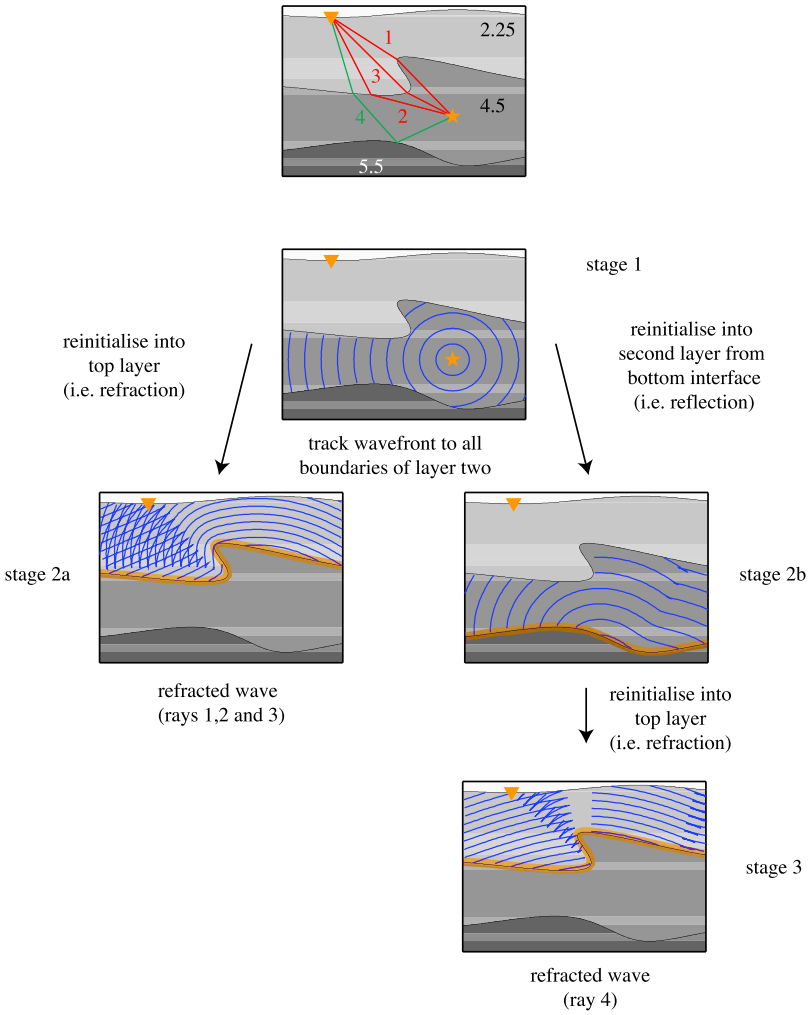

Figure 5. The steps of a multistage approach for the computation of ray paths for a direct wave (red rays) and a wave reflected from the bottom interface (green ray). Velocities (in km/s) for the three layers are given in the top diagram. Both path signatures share the wavefront emanating from the source in the middle layer. Note how the reflected and refracted wavefronts triplicate due to the shape of the interfaces and how the triplications can be propagated across interfaces. The interfaces from which the wavefront starts are highlighted in orange. The wavefront computed in stage 3 shows a gap due to the overturning middle interface, which splits the upcoming wavefront.

receiver lies inside the polygon, an arrival time needs to be calculated. The time and position of the two wavefront segments of the polygon is known and so the shortest distance from the receiver to each wavefront can be calculated. Using these two distances, an arrival time can be linearly interpolated. This scheme is similar to an approach advocated by *Vinje et al.* [1993].

[28] For applications such as seismic tomography the ray path has to be located for each arrival. A source-receiver ray path can be constructed in normal space by following the wavefronts back from the receiver to the source, once the wavefront propagation is finished. In order to backtrack rays across interfaces, the origin of the wavefront is needed. It may emanate from the source or be a reflection or refraction from an interface. This information can be obtained from the tree structure used to propagate the different wavefronts. The approach described here is capable of extracting a variety of ray paths for complex models, as shown in Figure 6. In this example, ray paths of multiply reflected and refracted waves are extracted for a structure which contains an overturning interface, a layer pinch-out, and an isolated body.

3. Potential Applications

[29] Multivalued traveltimes have the potential to benefit areas of seismology where traditionally

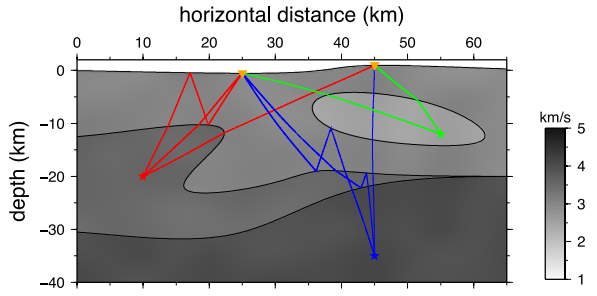

Figure 6. Complex model with a layer pinch-out, an isolated body, and an overturning interface. For three separate sources, ray paths with different path signatures are given in red, blue, and green.

only first arrival traveltimes have been used, for example traveltime tomography and migration of reflection data. Here, the emphasis is on applications in seismology outside the field of exploration, where wavefront construction is rarely used. A number of examples are presented which demonstrate the power of wavefront tracking, including body and surface wave tomography, global phase prediction, and synthetic seismogram generation using Gaussian beams. All computation times in this section are given for a Pentium 4 CPU running at 3.2 Ghz with 3 Gb of memory and a GNU/Linux operating system.

3.1. Gaussian Beams and Receiver Functions

[30] The Gaussian beam method [e.g., *Popov*, 1982; *Červený and Pšenčík*, 1984] is an asymptotic approach for the computation of seismograms in homogeneous and inhomogeneous media based on a combination of geometric ray concepts and elements of wave theory. Since high-frequency energy is considered to propagate along a ray, the wave equation can be solved in ray-centered coordinates. A parabolic approximation can be used to find the asymptotic local solution in the neighborhood of each ray. The wavefield at a receiver is then given by a superposition of the displacement field computed for the family of rays that pass near the receiver. One advantage of this technique is that Gaussian beams have no singularities at caustics in the spatial domain or pseudo-caustics in the wave number domain [*Nowack*, 2003] and therefore can automatically deal with phase distortions.

[31] *Stacy and Nowack* [2002] use the Gaussian beam method in two dimensions to model seismic attributes in a wide angle refraction study. In the field of reflection seismology, *Hill* [2001] discusses a Gaussian beam migration method, which is based on reversing the steps of Gaussian beam forward modeling. *Dunn and Forsyth* [2003] use a Gaussian beam method to predict observed packets of Love waves. It has also been used for modeling teleseismic *P* waves in three-dimensional structures [*Cormier*, 1987].

[32] Detailed descriptions of the Gaussian beam method for two-dimensional heterogeneous structures with interfaces have been given by *Červený and Pšenčík* [1984], *Červený et al.* [1982], and *Červený et al.* [1977]. In this work the focus is only on the enhancement of the Gaussian beam method by using wavefront tracking to identify the complete set of paths.

[33] The wavefront tracking approach allows the width of the ray fans in the Gaussian beam method to be precisely controlled (see Figure 7). Having extracted the ray paths for each arrival at a receiver, we know the ray parameters of rays hitting the surface close to the receiver. Since it is only these rays that contribute to the displacement field, one can shoot a narrow fan of rays and therefore avoid solving the dynamic and kinematic ray tracing equations for redundant rays. This also helps to avoid interference between the rays but still allows a waveform at the receiver to be constructed based on more than just the information along the kinematic ray path between source and receiver.

[34] In the following, a simple two-layered model is used to show that later arrivals contain additional information about structure and illustrate how this information influences the waveform. Figure 8a shows a structure with two layers and ray paths associated with an incoming plane wave. The *P* and *S* wave velocity increases linearly with depth in the upper layer and is constant in the lower layer.

[35] An incoming teleseismic *P* wave is represented by a plane wave with 200 nodes on the bicharacteristic strip and 250 × 250 nodes on the interface grid. A time step of 0.025 s is used. The incoming *P* wave is split at the interface into a *P* and *S* wave. In addition to the direct *P* wave and the *P* to *S* conversion, all reverberations of the incoming *P* wave which bounce once between the surface and the interface are computed. This means that in total 10 different phases are simulated. Owing to the velocity structure the wavefronts triplicate, and in addition to the 10 first arrivals associated with the 10 different phases, 30 later arrivals are also generated. Figure 8b illustrates, for the *P* to *S* conversion of the incoming plane wave, how later arrivals are generated due to the shape of

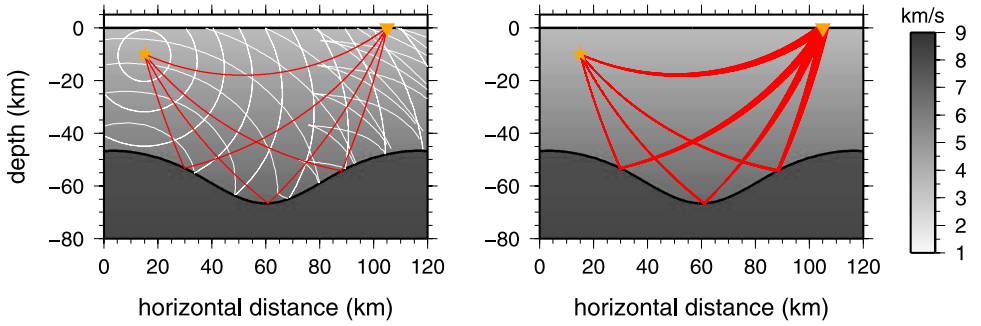

Figure 7. (left) Ray path information obtained by the wavefront tracking is used in the Gaussian beam method to (left) shoot only those rays that hit the surface in the vicinity of the receiver. Note that for illustration purposes, the ray fans are wider than those actually used for the computation of a synthetic seismogram.

the interface and the velocity contrast. The wavefront triplicates for this phase and three arrivals are generated.

[36] The Gaussian beam method is used to compute synthetic seismograms with an initial beam width of 0.005 $km^{1/2}$ and a peak angular frequency for the Ricker wavelet of $\omega_{peak} = 0.5$ rad s^{-1}. The computation time for the wavefront tracking and the calculation of a synthetic seismogram is 22 s. Figure 9a shows the resulting synthetic seismogram.

[37] In order to demonstrate how including later arrivals in the computation of the synthetic seismograms makes the waveform more sensitive to small changes in structure, the shape of the valley in the interface is perturbed. The bottom of the valley in the interface is defined by the depth of the control node at a horizontal distance of 25 km. Synthetic seismograms are now computed for different depths of the central interface node. Figure 9b shows the horizontal component of the waveform if only first arrivals of the different phases are used, and Figure 9c shows the horizontal component of the waveform if first and later arrivals are used. As the direct *P* wave does not triplicate, the wave packages associated with the first arrivals in the two seismograms have the same shape. The shape of the *P* to *S* conversion is, however, significantly different depending on whether first arrivals only or first and later arrivals are used, due to the triplication. Clearly, the waveform is more sensitive to changes in structure when both first and later arrivals are included, and hence the later arrivals contain additional structural information. This example suggests that the new technique may have potential in receiver function studies, where lateral heterogeneity can cause multipathing.

[38] Traditional Gaussian beam synthetics are computed using paths provided by initial value ray tracing, as it is usually argued that two-point ray tracing is not required [e.g., *Nowack*, 2003] due to

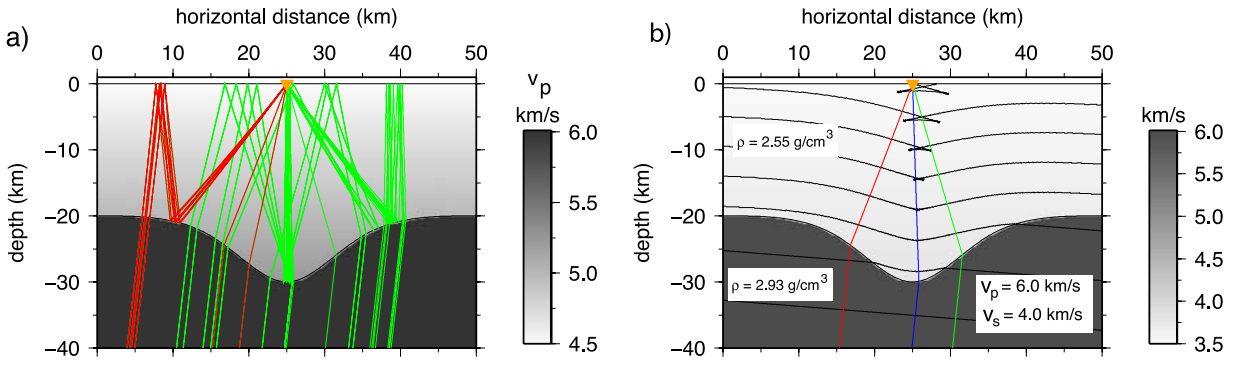

Figure 8. Ray paths for an incoming plane wave and its reverberations in the upper layer. (a) The first arrival ray paths for the different phases are plotted in red, and the ray paths for the later arrivals in green. (b) Ray paths and wavefronts for the *P* to *S* conversion of the incoming plane wave. The wavefront triplicates due to the shape of the interface and the velocity contrast. The velocity values shown in the figure are the *P* wave speed in the lower layer and the *S* wave speed in the upper layer. The ray path for the first arrival is red, for the second arrival is green, and for the third arrival is blue.

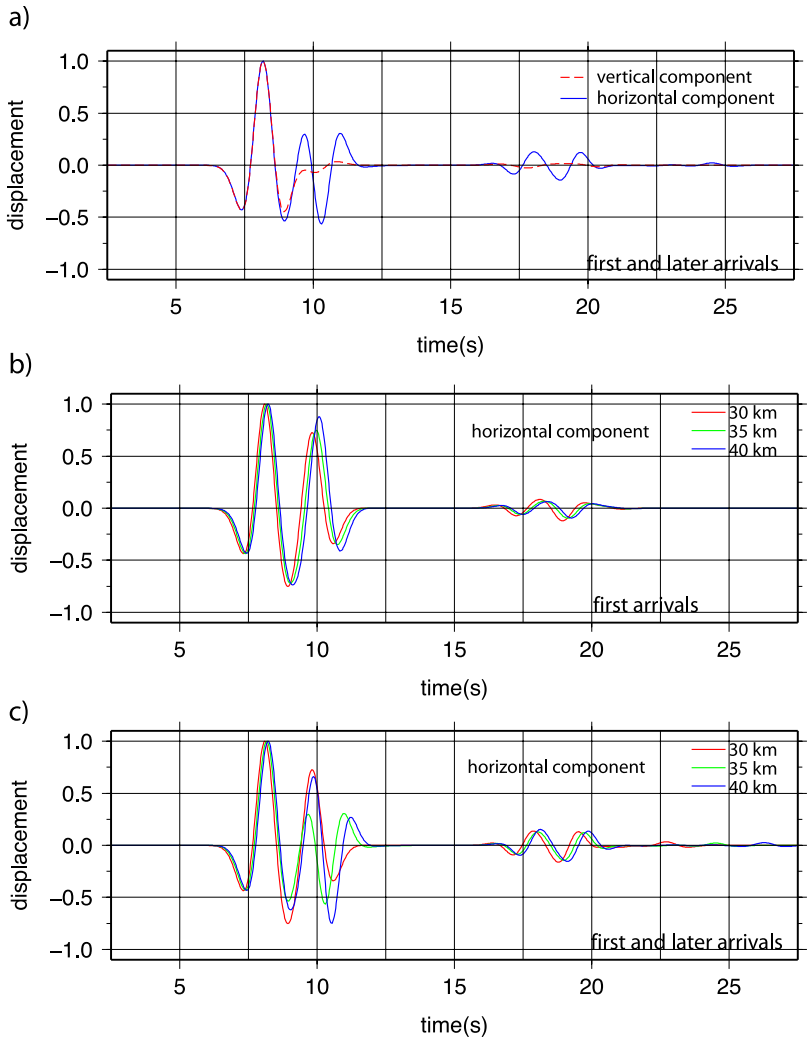

Figure 9. Gaussian beam synthetic seismograms for the structure shown in Figure 8. The components of the seismogram have been normalized. (a) Horizontal and vertical component of the synthetic seismogram. Horizontal component of the synthetic seismogram for different depths of the central interface control node (b) when only first arrivals of the different phases are used (i.e., red ray paths in in Figure 8a) and (c) when first and later arrivals of the different phases are used (i.e., red and green ray paths in Figure 8a).

finite beam width. However, in media exhibiting significant heterogeneity, the ability to adequately cover a region with initial value rays is much more challenging, and it is likely that only partial information will be used to construct the synthetic seismogram. Therefore, while the example of first-arrival synthetics in Figure 9b may not be what is normally arrived at in practice, it does represent one end-member solution possibility and contrasts significantly with the full multiarrival synthetic (Figure 9c).

3.2. Global Traveltime Example

[39] The *ak*135 model [*Kennett et al.*, 1995] is a one-dimensional reference model of the Earth. Accurate tables of arrival times (http://rses.anu.edu.au/seismology/ttsoft.html) are compared with solutions calculated using the wavefront tracking approach presented in this work. The computations are performed on a spherical Earth. This implies that no corrections for ellipticity are applied to either the reference values for the traveltime or the solutions computed using the wavefront tracking scheme. The model parameterization that is used allows for the description of complex models as illustrated earlier (Figure 6) in a Cartesian framework. To mimic a spherical medium, the basic idea is to sample the *ak*135 model on a Cartesian grid and describe the layered Earth using isolated bodies and overturning interfaces. Provided a high

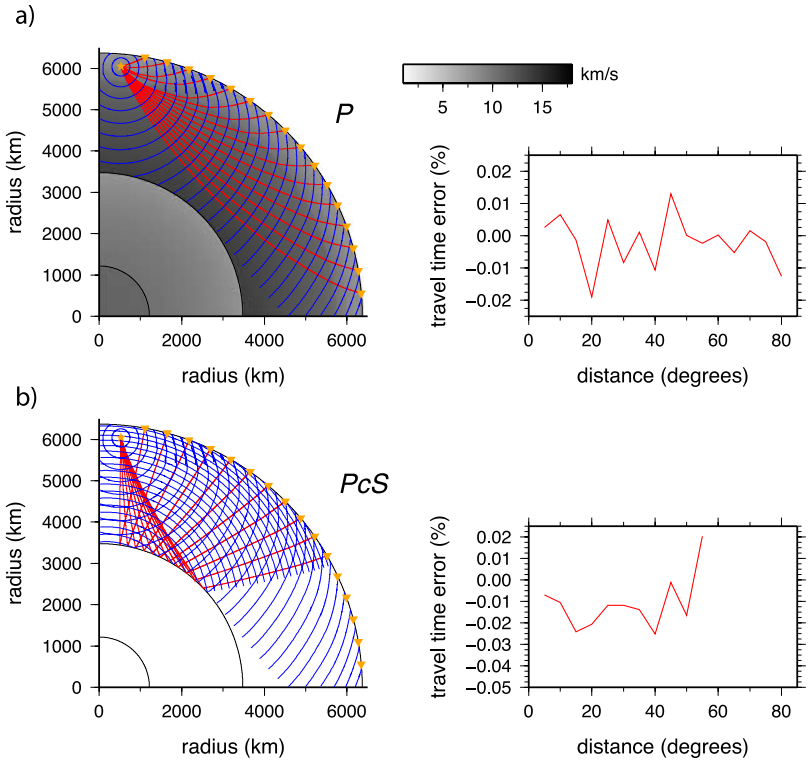

Figure 10. Ray paths, wavefronts, and relative traveltime error (a) for the direct *P* phase in the *ak*135 global model (computation time is 116 s) and (b) for the *PcS* phase (computation time is 99 s) in the *ak*135 global model.

enough grid resolution for the underlying Cartesian grid is used, the error associated with the conversion of the model from polar to Cartesian coordinates should be negligible. For an intermediate depth event (300 km) the traveltimes and ray paths for different global phases are computed. The traveltimes are compared with the reference traveltimes for the *ak*135 model. The core mantle boundary and the inner-outer core boundary are represented by explicit interfaces, and the grid spacing for the underlying velocity field is 5 km. Mantle discontinuities are not expressed by explicit interfaces. The time step is set to 0.2 s and 100 points are used to represent the bicharacteristic strip at the source. In this example the interface grid used in the tracking scheme is set at 1000 × 1000 nodes.

[40] The ray paths, wavefronts, and relative traveltime error for the direct *P* and *PcS* phases are shown in Figure 10. The relative traveltime error for the reflections from the core mantle boundary is slightly larger. In Figure 11, Gaussian distributed random numbers with a standard deviation of 2.5 km/s are created on a grid with a spacing of 400 km and then added to the *ak*135 Cartesian velocity grid using cubic B-splines. The position of the core mantle boundary is also perturbed in the depth direction using Gaussian random numbers with a standard deviation of 100 km. *P* and *PcP* phases are computed for this model. The structure gives rise to several occurrences of multipathing (see Figure 11) due to the shape of the core mantle boundary and velocity heterogeneities in the mantle.

[41] This example serves to demonstrate that wavefront tracking is not limited to computing traveltimes for local or regional models. One potential application might be in the imaging of the deep mantle near the boundary with the core, where the complex heterogeneity associated with the D" zone can produce multipathing. Another possibility is the prediction of later arrivals associated with sharp velocity gradients in the vicinity of upper mantle discontinuities [*Song et al.*, 2004]. The accuracy of the technique for the above examples is of the order of 0.1 s which is comparable to the accuracy achieved for global seismic phases when a graph and perturbation method are used [e.g., *Bijwaard and Spakman*, 1999]. Compared to conventional ray methods that account for lateral heterogeneity in the Earth [e.g., *Julian and Gubbins*, 1977; *Thurber and Ellsworth*, 1980] this

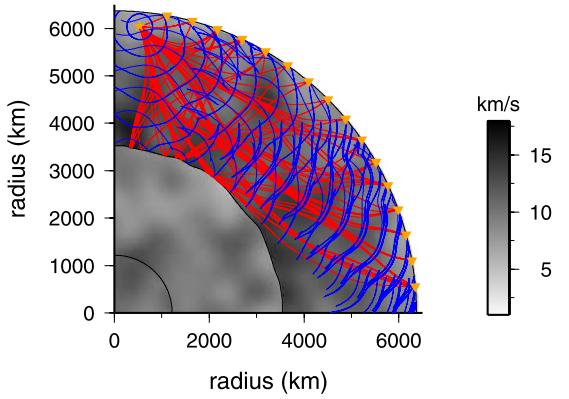

Figure 11. Wavefronts and ray paths for *P* and *PcP* phases computed for the *ak*135 model with Gaussian-distributed random noise added to the velocity field and core mantle boundary geometry. While the heterogeneity is unrealistically large it serves to demonstrate the robustness of the technique. The computation time required to predict the traveltimes alone is 77 s.

new approach has the advantage of robustness (as shown in Figure 11), and potentially, efficiency.

3.3. Multiarrival Tomography

[42] The inversion of first arrival traveltimes is undoubtedly the most popular technique for imaging subsurface seismic structure at all scales [e.g., *Nolet*, 1987; *Bregman et al.*, 1989; *Toomey et al.*, 1998; *Rawlinson et al.*, 2006; *Conder and Wiens*, 2006]. A comprehensive review of the methodology and its application has been given by *Rawlinson and Sambridge* [2003]. As discussed previously, later arrivals sample different parts of a structure when compared with first arrivals and therefore have the potential to contain additional information. This means that if they are used in seismic tomography, improved images should result. To investigate this possibility, two numerical tests are performed in which the results of first and multiarrival tomography are compared. The first test is a body wave example that attempts to recover velocity and interface structure simultaneously. In the second test, a smooth velocity model is reconstructed from surface wave traveltimes. A nonlinear iterative inversion procedure is used to solve the multiarrival tomography problem. The model perturbation is computed in this work using the subspace method, which has the advantage that the pseudo-inverse has to be computed for only a small matrix [e.g., *Kennett et al.*, 1988; *Williamson*, 1990; *Rawlinson and Sambridge*, 2003].

[43] It is important to emphasize that the existence of later arrivals is highly dependent on the character of the velocity structure. In a smooth velocity model, there is always a first arrival ray path between a source and a receiver, but later arrivals only exist if velocity gradients cause the wavefront to form a swallowtail. Here, later arrivals refer to the multipathing of transmissions and reflections and not just the first arrivals of reflections and refractions at discontinuities, which are sometimes used in tomography and also referred to as later arrivals [e.g., *Rawlinson and Sambridge*, 2003].

[44] In seismic tomography one typically begins with a simple, often one-dimensional, starting model [e.g., *Graeber et al.*, 2002; *Conder and Wiens*, 2006; *Rawlinson et al.*, 2006]. These models are unlikely to generate the multipathing observed in real data because of their simplicity. However, as the iterative inversion progresses and the model becomes more complex, later arrivals will gradually appear and be used to refine the solution. This means that during the iterative inversion procedure, the number of ray paths and hence data is not constant. As a consequence, the RMS (root mean square) data prediction error can actually increase as later arrivals appear for the first time and, at least initially, are not well described by the model.

[45] Once later arrivals start to be predicted during the iterative inversion procedure, they have to be correctly matched with observations. For example, given a particular source-receiver combination with five observed and three predicted arrivals, it may not be clear which two of the four observed later arrivals actually correspond to the predicted later arrivals. They are therefore matched according to their number, which means that the first predicted later arrival is assigned to the first observed later arrival and so on until there are no predictions or observations left. Although this may result in incorrect phase associations in some cases, the underlying improvement of the model at each iteration should gradually reduce this possibility. In the early stages of an iterative inversion procedure one would also expect the first arrivals to be the dominant influence in the reconstruction of model perturbations. Therefore a few mismatched later arrivals should not have a significant influence. As the solution converges toward the true model, additional later arrivals may appear, but they are more likely to be matched correctly.

[46] The main obstacle for multiarrival tomography is the correct identification of later arrivals in an

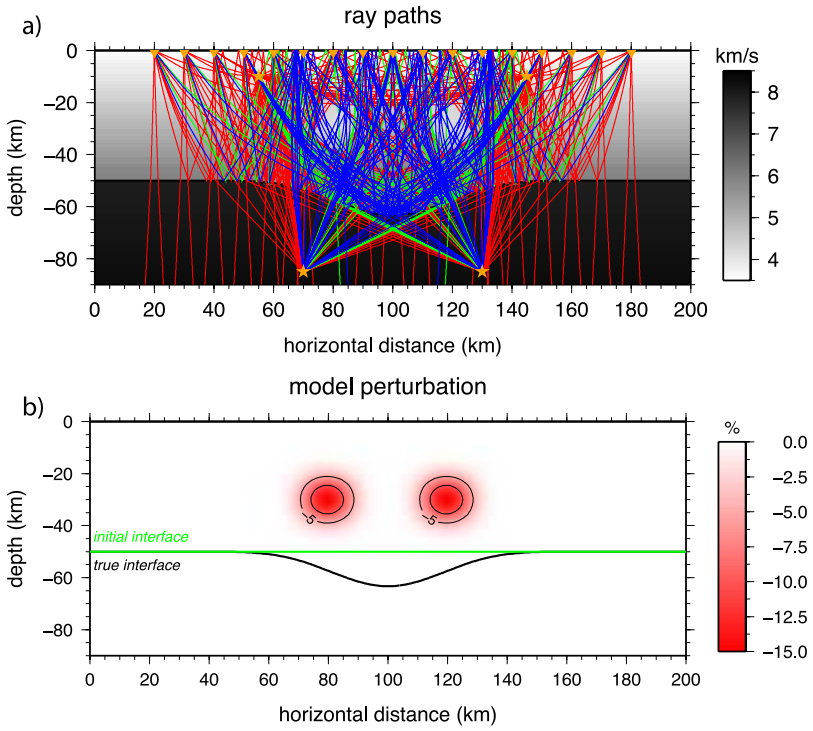

Figure 12. (a) Layered velocity model and associated paths used in the inversion test involving later arrivals. Ray paths corresponding to the first, second, and remaining later arrivals are plotted as red, green, and blue lines, respectively. Point sources are denoted by stars and receivers by triangles. Note that paths also emanate from two impinging plane wavefronts. (b) The interface perturbation and velocity anomalies that define the true model. The contour lines are plotted at 5% intervals.

observed seismogram. The Lagrangian solver used in this work can calculate the traveltime and the direction of the incoming ray for each arrival at a receiver. Using Gaussian beams, one can also compute synthetic seismograms for body waves. Considering that multipathing of surface waves is a frequently observed phenomenon [e.g., *Capon*, 1971], the most feasible step might be the use of a multiarrival scheme in surface wave tomography, or ambient noise tomography.

3.3.1. Body Wave Tomography Example

[47] In this numerical test the inversion is performed simultaneously for the velocity and interface structure of a two-layered model using (1) only first arrivals and (2) first and later arrivals. The true model (i.e., the model we try to recover) and the ray paths are shown in Figure 12a. Note how the later arrivals are clustered in the valley structure created by the downward deflection of the interface. For the two sources in the upper layer, the direct wave and the reflection from the interface are used, and for the two sources in the lower layer, the refracted wave and the associated multiple (i.e., reflected once between free surface and interface) are used. Two incoming plane waves which refract at the interface are also included. The number of observed arrivals is provided in Table 1. This forms our set of observed traveltimes for the synthetic model, which we will try to recover in an iterative inversion procedure.

[48] The synthetic test model is based on a depth-dependent background velocity field. In the upper layer the velocity at the surface is 3.0 km/s and increases with depth at a rate of 0.05 s^{-1}. In the lower layer, the velocity increases at a rate of 0.01 s^{-1} to 8.2 km/s at the bottom. The interface is

Table 1. Number of Observed Arrivals for the Test Problem Shown in Figure 12

	Observed Arrivals
First arrivals	170
Second arrivals	32
Third arrivals	32
Total (first, second, and third)	234
Fourth arrivals	12
Fifth arrivals	12
Sixth arrivals	2
Total (fourth, fifth, and sixth)	26

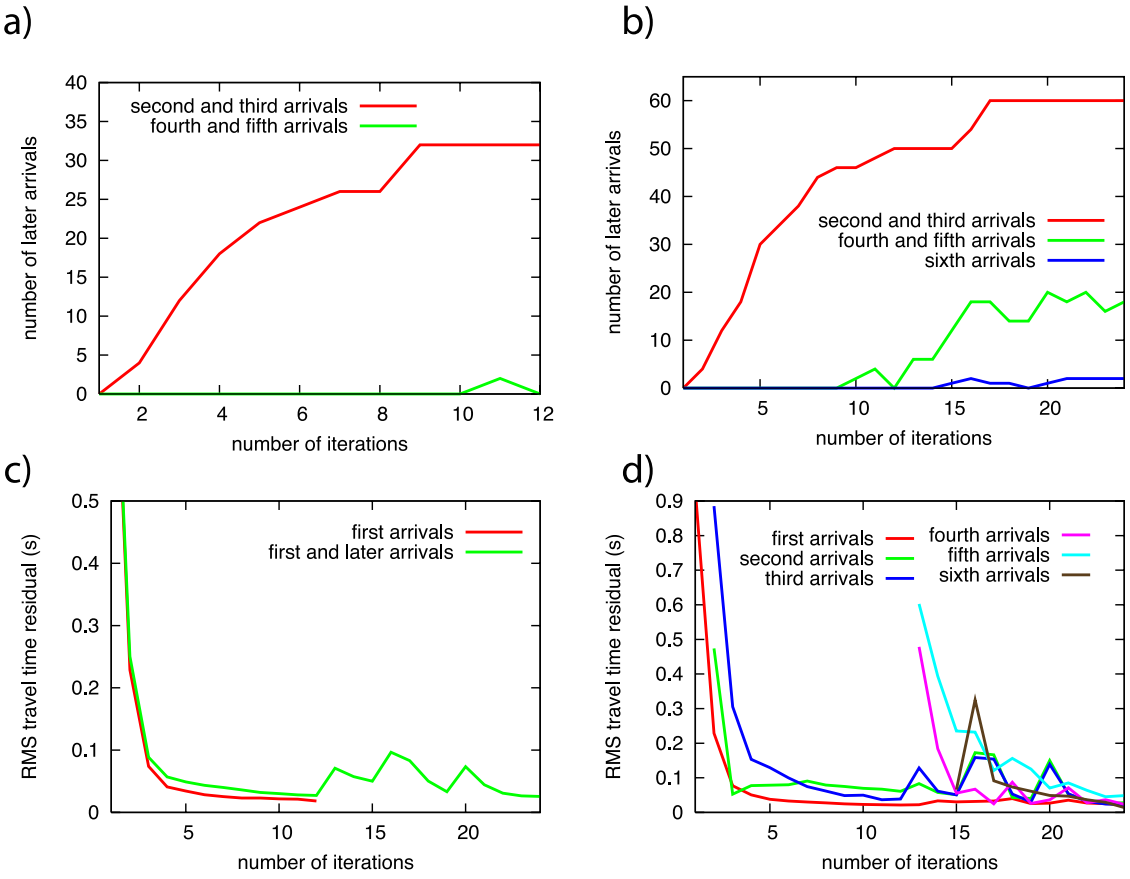

Figure 13. (a) Number of later arrivals as a function of iteration when only first arrivals are used during the iterative inversion procedure. (b) Number of later arrivals when first and later arrivals are used during the iterative inversion procedure. (c) RMS traveltime residuals for the two solutions. (d) RMS traveltime residuals for the different arrivals when first and later arrivals are used in the iterative inversion procedure.

given by a horizontal line. The spacing of the velocity grids is 10 km and the interface is defined using nine control nodes. A perturbation to both interface and velocity structure is then superimposed on the background model as shown in Figure 12b. There are two low-velocity anomalies (15% perturbation) in the upper layer and the central interface node is perturbed so that a valley is formed. The background velocity distribution is used as the initial model for the inversion procedure. A 12-dimensional subspace is used to compute the model perturbation and the iterative inversion procedure is stopped if the RMS value of the traveltime residuals falls below 0.02 s.

[49] When only first arrivals are used in the inversion, the final model does not generate any fourth, fifth, or sixth arrivals. In Figure 13a, second and third arrivals appear gradually up to the ninth step of the iterative inversion procedure. After the ninth iteration, the number of second and third arrivals is constant (32). It is interesting to note that the model used at iteration 11 generates two fourth and fifth arrivals. Figure 13b shows the number of later arrivals as a function of iteration when first and later arrivals are used in the inversion. Second and third arrivals appear after the first iteration, and once the perturbations are large enough, fourth, fifth, and sixth arrivals start to appear. The introduction or removal of later arrivals tends to be gradual rather than dramatic. The 60 predicted second and third arrivals are close to the observed number of 64. The 18 predicted fourth and fifth arrivals is also close to the observed number of 20; the two observed sixth arrivals are also predicted.

[50] The computation time for the iterative inversion procedure when only first arrivals are used is 20 min; this compares to 55 min when first and later arrivals are used. The multiarrival tomography takes significantly longer because of the larger number of iterations and the greater number of arrivals for which ray paths and Fréchet derivatives have to be computed.

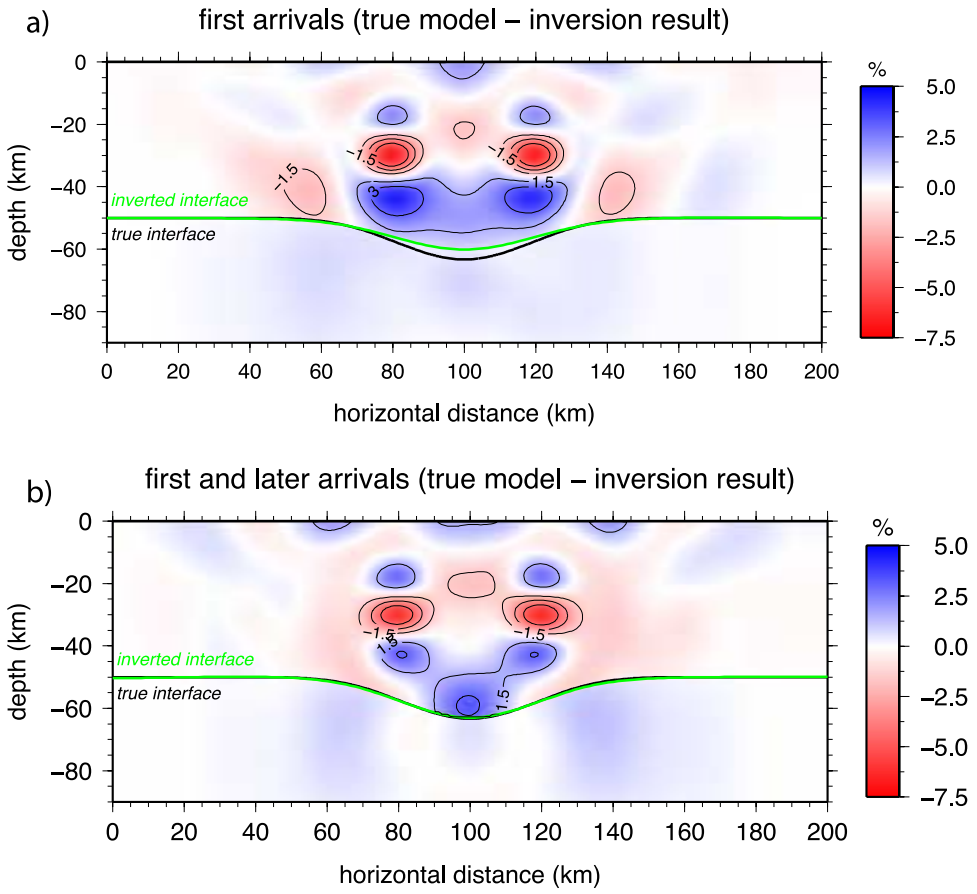

Figure 14. Relative error in percent between the true model and the inversion result (a) based on first arrivals and (b) based on first and later arrivals. Contour lines are plotted at 1.5% intervals.

[51] Figure 13c shows the RMS traveltime residuals or error for the two solution classes. When only first arrivals are used, the RMS value decreases monotonically. On the other hand, when first and later arrivals are used, the RMS error initially decreases, then increases as fourth, fifth, and sixth arrivals appear, before undulating for a few iterations and finally decreasing. This behavior is due to the appearance of fourth, fifth, and sixth arrivals, to which the structure has yet to be adjusted. In Figure 13d the RMS traveltime residuals for the different arrivals are plotted. It is important to note that the RMS value of the first arrivals decreases within the first 10 iterations and then stays relatively constant. Also in the first 10 iterations, the RMS value of the second arrivals decreases initially but then stays at a relatively large value. For the third arrivals the RMS value also decreases in the first 10 iterations but is smaller than for the second arrivals. When the fourth, fifth, and sixth arrivals are predicted for the first time, they show relatively large traveltime residuals. As they are taken into account during later steps of the iterative inversion procedure, the RMS value for second and third arrivals increases. Adjusting the structure for one class of later arrivals therefore appears to increase the misfit for another class. This behavior of the RMS value could also be due to a mismatch between the observed and predicted later arrivals for several source-receiver pairs (i.e., when the number of predicted arrivals is not equal to the number of observed arrivals, as discussed earlier). Only after the 20th step does the RMS value decrease for all later arrivals. Note that in Figure 13a fourth and fifth arrivals are predicted at the 10th and 11th iteration. They, however, do not appear in the plot of the RMS value (Figure 13d) of the different arrivals, due to the fact that there are no observations for these later arrivals.

[52] Figure 14a shows the difference between the inversion result and the true structure when only first arrivals are used in the inversion. The tradeoff between interface geometry and velocity anomaly is clearly not as well resolved compared to when both first and later arrivals are used (Figure 14b). If first arrivals are used, it takes 12 iterations to

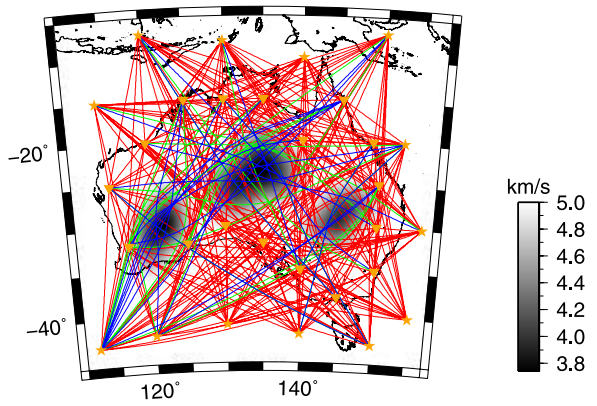

Figure 15. True velocity model and associated ray paths for surface wave tomography example. Ray paths corresponding to first, second, and remaining arrivals are plotted as red, green, and blue lines, respectively. Note how the later arrivals sample the low-velocity anomalies.

reduce the RMS value of the traveltime residual to less than 0.02 s, compared with 24 iterations, when first and later arrivals are used.

[53] In general it turns out that adding later arrivals makes the inverse problem much more nonlinear, which means that care must be taken to avoid instabilities in an iterative nonlinear approach.

3.3.2. Surface Wave Tomography Example

[54] The following example demonstrates the potential of multiarrival surface wave tomography. This is arguably a more realistic application than the previous example as surface wave multipathing is more readily identifiable in seismic records and ambient noise cross-correlations.

[55] The model is constructed using a background velocity of 5 km/s. Three distinct low-velocity anomalies (Figure 15) are then superimposed. One can see from Figure 15 that the first arrival ray paths are guided away from the large-amplitude low-velocity anomalies, compared to later arrivals. The structure generates 221 first and 66 later arrivals. Gaussian distributed random noise with a standard deviation of 0.15 s is added to the synthetic traveltimes to simulate the effects of observational uncertainty. These traveltimes are then used to recover the structure using the same nonlinear iterative inversion procedure described in the previous section. A model with a constant velocity of 5 km/s is used as the starting model. In the case of the first arrival tomography, the nonlinear iterative inversion is stopped when the RMS value for the traveltime residuals is below 0.15 s (i.e., the standard deviation of the Gaussian distributed random noise). The first arrival tomography requires 457 s of CPU time for 32 iterations. In the multiarrival tomography the iterative nonlinear inversion is stopped after the same number of iterations and requires 698 s of CPU time. The RMS value of the traveltime residuals is 0.196 s. An additional 30 iterations would decrease the RMS value by only 0.009 s.

[56] The differences between the inversion results and the true model are plotted for first arrival tomography in Figure 16a and for multiarrival tomography in Figure 16b. As is the case for the body wave tomography, multiarrival tomography leads to a better recovery of the low-velocity anomalies compared with first arrival tomography. This is especially the case near the westernmost

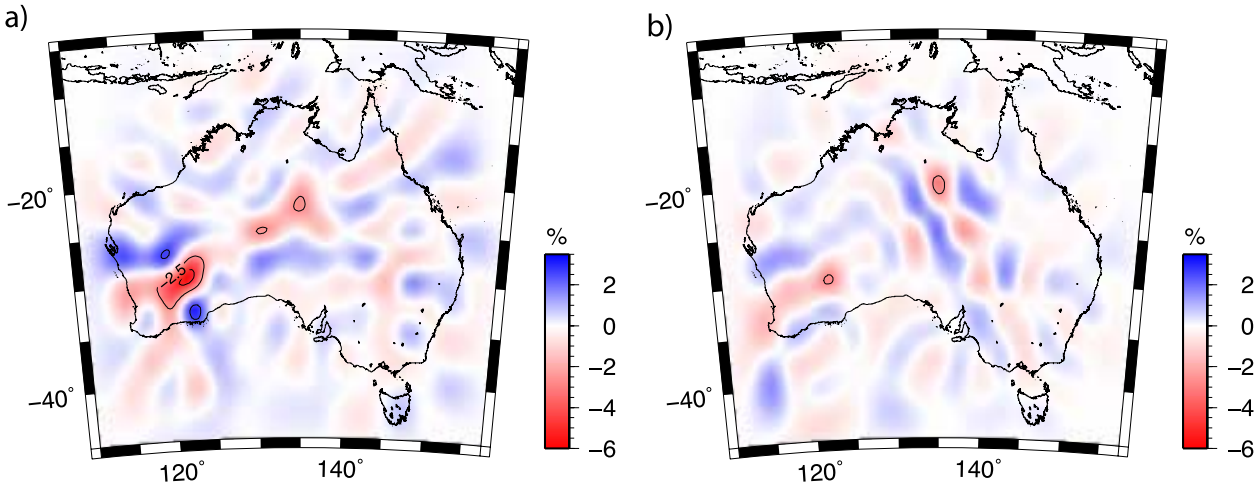

Figure 16. Relative difference (true model minus inversion result) (a) when only first arrivals and (b) when first and later arrivals are used to recover structure. Contour lines are plotted at 2.5% intervals.

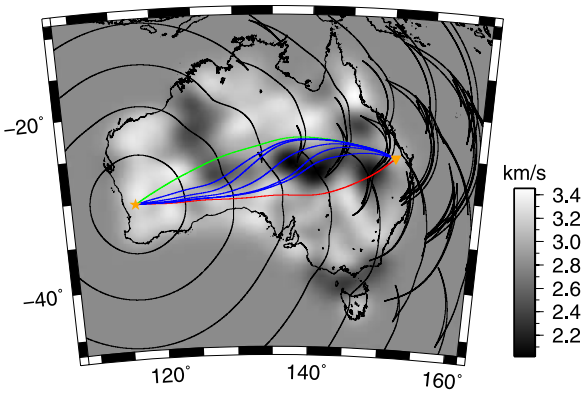

Figure 17. Rayleigh wave group velocity with a frequency of 0.2 Hz obtained from ambient noise first arrival tomography [*Saygin*, 2007]. For the given source receiver pair up to 7 arrivals are predicted by multiarrival wavefront tracking.

anomaly, where using first arrivals introduces spurious fast anomalies surrounding the low-velocity anomaly. The error amplitude in the center of the model is slightly higher for multiarrival tomography. A possible explanation for this is that due to the increased nonlinearity the iterative nonlinear inversion scheme has found only a local minimum of the objective function and not the global minimum. In summary multiarrival tomography leads overall to a better recovery of structure given the same number of iterations despite a slightly larger RMS value for the traveltime residuals.

[57] Figure 17 shows multipathing between two stations in a velocity model for Rayleigh waves with a frequency of 0.2 Hz obtained from ambient noise data. The velocity model was obtained using only first arrival paths between stations [*Saygin*, 2007]. Figure 18 shows the long-term cross-correlation of the ambient noise between the two stations. The predicted traveltime for the first, second, third, and later arrivals are marked. Relative amplitudes due to geometrical spreading have been predicted for each arrival by keeping track of the change in distance between each node and its neighbors as the wavefront propagates. In the cross-correlated noise one can clearly recognize the second arrival (green), which fits the data surprisingly well compared to the first arrival. Predicted third and later arrivals show a lower amplitude than the corresponding observations and arrive earlier than the maximum amplitude of the last wave packages. However, considering the clustering of these arrivals it is probable that interference between the wavelets for each arrival is responsible for this effect. In addition to relative amplitudes, the direction of the incoming wave package could also be used to identify later arrivals for three component recordings. This example clearly demonstrates that it is possible to discriminate between later arrivals in an observational data set, thereby making multiarrival tomography a realistic proposition for some classes of study.

4. Discussion and Conclusions

[58] The scheme presented in this work for wavefront tracking in two dimensions can be used as an alternative to first arrival schemes for the computation of traveltimes in heterogeneous two-dimensional media, with the added benefit that later arrivals are included. Although Lagrangian wavefront tracking techniques in two dimensions have been developed previously [e.g., *Lambaré et al.*, 1992; *Vinje et al.*, 1993], our scheme is different in that the wavefront is unfolded into reduced phase space, where it stays locally smooth. The ability to remove points dynamically during the propagation process leads to greater efficiency and further distinguishes the new scheme from previous work in the field. While we have extended the method to three-dimensional continuous media using sophisticated surface refinement techniques that were developed in computer graphics [e.g., *Zorin et al.*, 1996; *Garland and Heckbert*, 1997], it is beyond the scope of this paper to consider such techniques here. Besides, the particular applications in seismology that we have presented do not require three-dimensional wavefront tracking.

[59] In addition to improving the basic wavefront tracking technique, a variety of application in solid earth seismology are investigated for the first time. Previously the focus has been on applications in the field of exploration geophysics [e.g., *Vinje et al.*, 1993; *Lambaré et al.*, 1996; *Vinje et al.*, 1999; *Xu and Lambaré*, 2004]. The suite of examples

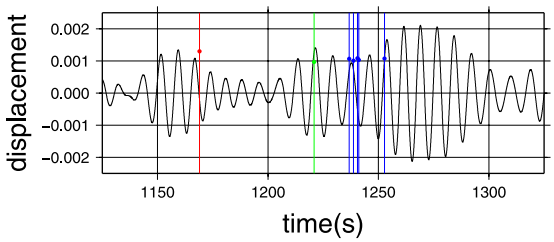

Figure 18. The extracted Green's function for Rayleigh waves. The different arrivals predicted by multipathing are marked by the red (first arrival), green (second arrival), and blue (third and later arrivals) lines. The points mark the relative amplitudes based on geometrical spreading.

presented here show that wavefront tracking can be a valuable tool at local, regional, and global scales. In the latter case multipathing global phases (*P*, *PcP*, etc.) were efficiently tracked through a heterogeneous Earth.

[60] The structure sampled by a later arriving ray path not only influences the traveltime but also manifests in the amplitude and phase shifts across interfaces. All this information can be incorporated into a synthetic seismogram using the Gaussian beam method. The ray paths obtained by the Lagrangian wavefront tracker are used to aim narrow fans of rays at the surface near the receiver. These rays are used in the Gaussian beam method to compute synthetic seismograms and the impulse response of structure beneath a receiver from teleseismic arrivals (i.e., a receiver function).

[61] Synthetic tests clearly show that velocity and interface structure can be recovered more accurately when later arrivals are exploited in addition to first arrivals. However, if later arrivals are used in seismic tomography, the inverse problem becomes much more nonlinear. An iterative nonlinear procedure may therefore fail to find the global minimum. On the other hand, if later arrivals are used, the global minimum of the misfit function is likely to be better defined. A two step procedure, in which the solution model is initially obtained using only first arrivals, before adding later arrivals in a second inversion step, may be the best approach. In general it is still possible that the solution obtained from first arrivals only may not be sufficiently close to the global minimum to allow the effective inclusion of later arrivals. The solution to the nonlinearity of the multiarrival seismic tomography problem therefore might lie in the use of a direct search method [e.g., *Gill et al.*, 1981; *Kirkpatrick et al.*, 1983; *Whitley*, 1994]. One benefit of these nonlinear techniques is that there would be no need to calculate ray paths, which would decrease the computation time of the forward problem. Even so, they would only be practical for problems with up to several hundred unknowns; beyond this, direct search methods become computationally unfeasible. Observations of surface wave multipathing are common [e.g., *Capon*, 1971] and given that the number of unknowns in surface wave tomography can be relatively small [e.g., *Fishwick et al.*, 2005], it might be easier to exploit surface wave rather than body wave data.

[62] The next logical step with the two-dimensional wavefront construction technique is to use it in conjunction with real data. Two promising applications are receiver function analysis and surface wave tomography/ambient noise tomography. In receiver function analysis, the impulse response function may contain later arrivals due to lateral variations in structure. If these later arrivals can be predicted, they could be used as additional constraints. Ambient noise tomography results for the Australian continent suggest that there is severe multipathing for certain station pairs. This multipathing can be observed in the long term cross-correlation of the array data [*Saygin*, 2007], as shown in Figure 18. If this information could be extracted routinely, then it would present an ideal opportunity to evaluate the new multiarrival tomography technique with observational data.

Acknowledgments

[63] J. Hauser was supported by ARC Discovery Project DP0451133 and N. Rawlinson by ARC Discovery Project DP0556282. M. Kendall and an anonymous reviewer are thanked for their insightful comments, which substantially improved the paper.

References

Aki, K., and P. G. Richards (2002), *Quantitative Seismology*, 2nd ed. Univ. Sci. Books, Sausalito, Calif.

Benamou, J. D. (1999), Numerical solution of the high frequency asymptotic expansion for the scalar wave equation, *Commun. Pure Appl. Math.*, *52*(11), 1443–1475.

Bijwaard, H., and W. Spakman (1999), Fast kinematic ray tracing of first- and later-arriving global seismic phases, *Geophys. J. Int.*, *139*(2), 359–369.

Bregman, N., R. Bailey, and C. Chapman (1989), Crosshole seismic tomography, *Geophysics*, *54*(2), 200–215.

Bukchin, B., T. Yanovskaya, J. Montagner, A. Mostinskiy, and E. Beucler (2006), Surface wave focusing effects: Numerical modeling and statistical observations, *Phys. Earth Planet. Inter.*, *155*(3-4), 191–200.

Buske, S., and U. Kästner (2004), Efficient and accurate computation of seismic travel times and amplitudes, *Geophys. Prospect.*, *52*(4), 313–322.

Capon, J. (1971), Comparison of Love- and Rayleigh-wave multipath propagation at LASA, *Bull. Seismol. Soc. Am.*, *61*(5), 1327–1344.

Červený, V. (2001), *Seismic Ray Theory*, 1st ed., Cambridge Univ. Press, Cambridge, U. K.

Červený, V., and I. Pšenčík (1984), Gaussian beams in elastic 2-D laterally varying layered structures, *Geophys. J. R. Astron. Soc.*, *78*(1), 65–91.

Červený, V., I. Molotkov, and I. Pšenčík (1977), *Ray Method in Seismology*, 1st ed. Charles Univ. Press, Prague.

Červený, V., M. Popov, and I. Pšenčík (1982), Computation of wave fields in inhomogeneous media - Gaussian beam approach, *Geophys. J. R. Astron. Soc.*, *70*(1), 109–128.

Chapman, C. (1985), Ray theory and its extensions - WKBJ and Maslov seismograms, *J. Geophys.*, *58*(1–3), 27–43.

Chapman, C. (2004) *Fundamentals of Seismic Wave Propagation*, Cambridge Univ. Press, Cambridge, U. K.

Conder, J. A., and D. A. Wiens (2006), Seismic structure beneath the Tonga arc and Lau back-arc basin determined from joint Vp, Vp/Vs tomography, *Geochem. Geophys. Geosyst.*, *7*, Q03018, doi:10.1029/2005GC001113.

Cormier, V. (1987), Focusing and defocusing of teleseismic P waves by known three-dimensional structure beneath Pahute Mesa, Nevada test site, *Bull. Seismol. Soc. Am.*, *77*(5), 1688–1703.

de Kool, M., N. Rawlinson, and M. Sambridge (2006), A practical grid-based method for tracking multiple refraction and reflection phases in three-dimensional heterogeneous media, *Geophys. J. Int.*, *167*(1), 253–270.

Dunn, R., and D. Forsyth (2003), Imaging the transition between the region of mantle melt generation and the crustal magma chamber beneath the southern east pacific rise with short-period Love waves, *J. Geophys. Res.*, *108*(B7), 2352, doi:10.1029/2002JB002217.

Ettrich, N., and D. Gajewski (1996), Wavefront construction in smooth media for prestack depth migration, *Pure Appl. Geophys.*, *148*(3/4), 481–502.

Fatemi, E., B. Engquist, and S. Osher (1995), Numerical solution of the high frequency asymptotic expansion for the scalar wave equation, *J. Comput. Phys.*, *120*(1), 145–155.

Fishwick, S., B. L. N. Kennett, and A. M. Reading (2005), Contrasts in lithospheric structure within the Australian craton - insights from surface wave tomography, *Earth Planet. Sci. Lett.*, *231*(3-4), 163–176.

Garland, M., and P. S. Heckbert (1997), Surface simplification using quadric error metrics, in *Proceedings of the 24th Annual Conference on Computer Graphics and Interactive Techniques*, edited by G. S. Owen, T. Whitted, and B. Mones-Hattal, pp. 209–216, ACM Press, New York.

Geoltrain, S., and J. Brac (1993), Can we image complex structures with first arrival travel time?, *Geophysics*, *58*(4), 564–575.

Gill, P. E., W. Murray, and M. H. Wright (1981), *Practical Optimization*, Academic, London.

Graeber, F. M., G. A. Houseman, and S. A. Greenhalgh (2002), Regional teleseismic tomography of the western Lachlan Orogen and the Newer Volcanic Province, southeast Australia, *Geophys. J. Int.*, *149*(2), 249–266.

Gray, S. H., and W. P. May (1994), Kirchhoff migration using eikonal equation travel-times, *Geophysics*, *59*(5), 810–817.

Haines, E. (1994), Point in polygon strategies, in *Graphics Gems IV*, edited by P. S. Heckbert, pp. 24–46, AP Prof., Boston, Mass.

Hammer, P. T. C., L. M. Dorman, J. A. Hildebrand, and B. D. Cornuelle (1994), Jasper Seamount structure: Seafloor seismic refraction tomography, *J. Geophys. Res.*, *99*(B4), 6731–6752.

Hill, N. (2001), Prestack Gaussian-beam depth migration, *Geophysics*, *66*(4), 1240–1250.

Julian, B. R., and D. Gubbins (1977), Three-dimensional seismic ray tracing, *J. Geophys.*, *43*(1), 95–113.

Kennett, B. L. N., M. Sambridge, and P. R. Williamson (1988), Subspace methods for large scale inverse problems involving multiple parameter classes, *Geophys. J. Int.*, *94*(2), 237–247.

Kennett, B. L. N., E. R. Engdhal, and R. Buland (1995), Constraints on seismic velocities in the Earth from travel times, *Geophys. J. Int.*, *122*(1), 108–124.

Kim, S., and R. Cook (1999), 3-D traveltime computation using second-order ENO scheme, *Geophysics*, *64*(6), 1867–1876.

Kirkpatrick, S., C. D. Gelatt Jr., and M. P. Vecchi (1983), Optimization by simulated annealing, *Science*, *220*(4598), 671–680.

Lambaré, G., J. Virieux, R. Madariaga, and S. Jin (1992), Iterative asymptotic inversion in the accoustic approximation, *Geophysics*, *57*(9), 1138–1154.

Lambaré, G., P. S. Lucio, and A. Hanyga (1996), Two-dimensional multivalued traveltime and amplitude maps by uniform sampling of a ray field., *Geophys. J. Int.*, *125*(2), 584–598.

Lucio, P. S., G. Lambaré, and A. Hanyga (1996), 3D multivalued travel time and amplitude maps, *Pure Appl. Geophys.*, *148*(3-4), 449–479.

Nolet, G. (1987), *Seismic Tomography: With Applications in Global Seismology and Exploration Geophysics*, Springer, New York.

Nowack, R. L. (2003), Calculation of synthetic seismograms with gaussian beams, *Pure Appl. Geophys.*, *160*, 487–507.

Osher, S., L. T. Cheng, M. Kang, Y. Shim, and Y. H. Tsai (2002), Geometric optics in a phase-space-based level set and Eulerian framework, *J. Comput. Phys.*, *179*(2), 622–648.

Pereyra, V., W. H. K. Lee, and H. B. Keller (1980), Solving two-point seismic-ray tracing problems in a heterogeneous medium. Part 1. A general adaptive finite difference method, *Bull. Seismol. Soc. Am.*, *70*(1), 79–99.

Popov, M. (1982), A new method of computation of wave fields using Gaussian beams, *Wave Motion*, *4*, 85–97.

Press, H. W., S. A. Teukolsky, W. T. Vetterling, and B. P. Flannery (1992), *Numerical Recepies in Fortran*, 2nd ed., Cambridge Univ. Press, Cambridge, U. K.

Rawlinson, N., and M. Sambridge (2003), Seismic traveltime tomography of the crust and lithosphere, *Adv. Geophys.*, *46*, 81–198.

Rawlinson, N., and M. Sambridge (2004a), Wave front evolution in strongly heterogeneous layered media using the fast marching method, *Geophys. J. Int.*, *156*(3), 631–647.

Rawlinson, N., and M. Sambridge (2004b), Multiple reflection and transmission phases in complex layered media using a multistage fast marching method, *Geophysics*, *69*(5), 1338–1350.

Rawlinson, N., A. M. Reading, and B. L. N. Kennett (2006), Lithospheric structure of Tasmania from a novel form of teleseismic tomography, *J. Geophys. Res.*, *111*, B02301, doi:10.1029/2005JB003803.

Rawlinson, N., J. Hauser, and M. Sambridge (2007), Seismic ray tracing and wavefront tracking in laterally heterogeneous media, *Adv. Geophys.*, *49*, 203–267.

Sambridge, M., and B. L. N. Kennett (1990), Boundary value ray tracing in a heterogeneous medium: A simple and versatile algorithm, *Geophys. J. Int.*, *101*(1), 157–168.

Saygin, E. (2007), Seismic receiver and noise correlation based studies in australia, Ph.D. thesis, Res. Sch. of Earth Sci. Aust. Natl. Univ., Canberra, ACT, Australia.

Sethian, J. A., and A. M. Popovici (1999), 3-D traveltime computation using the fast marching method, *Geophysics*, *64*(2), 516–523.

Song, T. A., D. V. Helmberger, and S. P. Grand (2004), Low-velocity zone atop the 410-km seismic discontinuity in the northwestern United States, *Nature*, *427*, 530–533.

Stacy, S., and R. Nowack (2002), Modeling of wide-angle seismic attributes using the Gaussian beam method, *Stud. Geophys. Geod.*, *46*(4), 667–690.

Steck, L. K., C. H. Thurber, M. Fehler, W. J. Lutter, P. M. Roberts, W. S. Baldridge, D. G. Stafford, and R. Sessions (1998), Crust and upper mantle P wave velocity structure beneath Valles caldera, New Mexico: Results from the Jemez teleseismic tomography experiment, *J. Geophys. Res.*, *103*(B10), 24,301–24,320.

Sun, Y. (1992), Computation of 2D multiple arrrival traveltime fields by an interpolative shooting method, in *Technical Program Expanded Abstracts*, vol. 11, pp. 1320–1323, Soc. for Explor. Geophys., Tulsa, Okla.

Thurber, C. H. (1983), Earthquake locations and three-dimensional crustal structure in the Coyote Lake area, central California, *J. Geophys. Res.*, *88*(B10), 8226–8236.

Thurber, C. H., and W. L. Ellsworth (1980), Rapid solution of ray tracing problems in heterogeneous media, *Bull. Seismol. Soc. Am.*, *70*(4), 1137–1148.

Toomey, D. R., W. S. D. Wilcock, S. C. Solomon, W. C. Hammond, and J. A. Orcutt (1998), Mantle seismic structure beneath the MELT region of the East Pacific rise from P and S wave tomography, *Science*, *280*(5367), 1224–1227.

van Trier, J., and W. W. Symes (1991), Upwind finite-difference calculation of traveltimes, *Geophysics*, *56*(6), 812–821.

Velis, D. R., and T. J. Ulrych (1996), Simulated annealing two-point ray tracing, *Geophys. Res. Lett.*, *23*(2), 201–204.

Vidale, J. E. (1988), Finite-difference calculation of traveltimes, *Bull. Seismol. Soc. Am.*, *78*(6), 2062–2076.

Vinje, V., E. Iversen, and H. Gjøystdal (1993), Travel-time and amplitude estimation using wave-front construction, *Geophysics*, *58*(8), 1157–1166.

Vinje, V., K. Åstebøl, E. Iversen, and H. Gjøystdal (1999), 3-D ray modeling by wavefront construction in open models, *Geophysics*, *64*(6), 1912–1919.

Virieux, J., and F. Farra (1991), Ray tracing in 3-D complex isotropic media: An analysis of the problem, *Geophysics*, *56*(12), 2057–2069.

Whitley, D. L. (1994), A genetic algorithm tutorial, *Stat. Comput.*, *4*(2), 65–85.

Williamson, P. R. (1990), Tomographic inversion in reflection seismology, *Geophys. J. Int.*, *100*(2), 255–274.

Xu, S., and G. Lambaré (2004), Fast migration/inversion with multivalued rayfields: Part 1 - Method, validation test, and application in 2D to Marmousi, *Geophysics*, *69*(5), 1311–1319.

Zelt, C. A., and R. M. Ellis (1988), Practical and efficent ray tracing in two-dimensional media for rapid traveltime and amplitude forward modelling, *Can. J. Explor. Geophys.*, *24*(1), 16–31.

Zorin, D., P. Schroeder, and W. Sweldens (1996), Interpolating subdivision for meshes with arbitrary topology, in *Proceedings of the 24th Annual Conference on Computer Graphics and Interactive Techniques*, edited by G. S. Owen, T. Whitted, and B. Mones-Hattal, pp. 189–192, ACM Press, New York.